

Two superconducting thin films systems with potential integration of different quantum functionalities

Snehal Mandal¹, Biplab Biswas¹, Suvankar Purakait², Anupam Roy³, Biswarup Satpati², Indranil Das² and B. N. Dev¹

¹ Centre for Quantum Engineering, Research and Education, TCG-CREST, EM Block, Sector-V, Salt Lake, Kolkata 700091, India.

² Saha Institute of Nuclear Physics, 1/AF, Bidhannagar, Kolkata 700064, India.

³ Dept. of Physics, Birla Institute of Technology Mesra, Ranchi, Jharkhand 835215, India.

E-mail: bhupen.dev@gmail.com

Abstract. Quantum computation based on superconducting circuits utilizes superconducting qubits with Josephson tunnel junctions. Engineering high-coherence qubits requires materials optimization. In this work, we present two superconducting thin film systems, grown on silicon (Si), and one obtained from the other via annealing. Cobalt (Co) thin films grown on Si were found to be superconducting [EPL 131 (2020) 47001]. These films also happen to be a self-organised hybrid superconductor/ferromagnet/superconductor (S/F/S) structure. The S/F/S hybrids are important for superconducting π -qubits [PRL 95 (2005) 097001] and in quantum information processing. Here we present our results on the superconductivity of a hybrid Co film followed by the superconductivity of a CoSi_2 film, which was prepared by annealing the Co film. CoSi_2 , with its $1/f$ noise about three orders of magnitude smaller compared to the most commonly used superconductor aluminium (Al), is a promising material for high-coherence qubits. The hybrid Co film revealed superconducting transition temperature $T_c = 5$ K and anisotropy in the upper critical field between the in-plane and out-of-plane directions. The anisotropy was of the order of ratio of lateral dimensions to thickness of the superconducting Co grains, suggesting a quasi-2D nature of superconductivity. On the other hand, CoSi_2 film showed a T_c of 900 mK. In the resistivity vs. temperature curve, we observe a peak near T_c . Magnetic field scan as a function of T shows a monotonic increase in intensity of this peak with temperature. The origin of the peak has been explained in terms of parallel resistive model for the particular measurement configuration. Although our CoSi_2 film contains grain boundaries, we observed a perpendicular critical field of 15 mT and a critical current density of 3.8×10^7 A/m², comparable with epitaxial CoSi_2 films.

Keywords: Superconductivity, upper critical field, critical current, van der Pauw, inhomogeneity, coherence length

1. Introduction

Superconductivity plays a pivotal role in quantum technology, especially in quantum computers. The basic unit of a quantum computer is a quantum bit (or qubit), which can be implemented via several physical platforms. However, superconducting qubit is one of the most promising approaches towards building a scalable fault-tolerant quantum computer [1, 2]. Superconducting qubit technology uses several superconducting materials, such as Al, Nb, Ta etc. for the fabrication of qubits, capacitor pads and resonators. One of the major aims of materials research in this area is to develop superior qubits with longer decoherence time. The main component of a superconducting qubit is a Josephson junction (JJ), which is a superconductor/insulator/superconductor (S/I/S) heterostructure [3]. Although, several superconductors are used for building superconducting quantum computers, Al is the most widely used superconducting material for the fabrication of qubits and quantum processors. Aluminum-based qubits use Al/AlO_x/Al heterostructures as JJs. Since the quantum states are intrinsically fragile, interactions of qubits with the environment result in various sources of noise which lead to decoherence. Suppressing decoherence, or increasing decoherence time, involves a synchronous optimization of both electromagnetic design and materials quality [4]. Besides the improvement of qubit design and microwave engineering, it is desirable to use superconductors with superior material properties. One important source of noise, responsible for qubit decoherence, is the $1/f$ noise [4] originating from the interfaces and surfaces of the materials and heterostructures used for fabricating the qubits. Recently it was shown that cobalt disilicide (CoSi₂), a superconductor with comparable supercon-

ducting transition temperature (T_c) to that of Al [5], has two to three orders of magnitude less $1/f$ noise compared to Al. It was conjectured that CoSi₂ films may provide superior qubits with longer decoherence time compared to Al [5].

CoSi₂ has already been used for decades as metallic contacts in semiconductor technology [6, 7]. CoSi₂ is usually produced by depositing thin films of cobalt (Co) on silicon (Si) followed by post-deposition annealing [6, 8], or by directly depositing Co on hot Si substrates [9, 10]. Out of these two materials - Co and CoSi₂ - although CoSi₂ is a superconductor [5, 11], Co was neither known nor expected to be a superconductor as cobalt is a ferromagnetic metal, and materials possessing long range magnetic order do not exhibit superconductivity [12]. In some cases, such ferromagnetic materials, for example iron (Fe), can show superconductivity under high pressure [13]. However, bulk Co was not shown to be a superconductor under any condition. Very recently, superconductivity was discovered in Co thin films grown on Si [14]. Normal Co has a hexagonal close packed (hcp) crystal structure and is ferromagnetic. In the thin films, grown on clean Si substrates, a high-density non-magnetic (HDNM) face-centered cubic (fcc) phase of Co was found to have grown [15, 16]. While normal Co is not superconducting, this HDNM phase of Co is superconducting [14]. Earlier, theoretically it was predicted that at a high-density the fcc phase of Co would lose magnetism [17], although no superconductivity was predicted. However, the theoretical work carried out together with the experimental discovery of superconductivity in Co shows that at certain densities of fcc Co, it becomes non-magnetic as well as superconducting, and a detailed phase diagram has been produced. This phase dia-

gram shows the range of densities and strains in the thin films for which superconductivity would be observed [14]. Another interesting aspect of these Co films is that the whole film is not superconducting. The films have a self-organised hybrid three-layer structure – HDNM-Co/Normal-Co/HDNM-Co [15, 16]. While the normal-Co is a ferromagnet (F), the HDNM-Co layers are superconductors (S). Thus, the Co films have an S/F/S hybrid structure. Such S/F/S hybrid structures have superconducting-spintronic and other applications in quantum technology, such as in quantum information processing [18, 19]. S/F/S structures have also shown $0-\pi$ quantum phase transition [20]. An S/F/S structure forms a ferromagnetic JJ (or π -JJ), which can be used to fabricate a superconducting π -qubit with a long decoherence time. Such a superconducting π -qubit may be a superconducting ring with one π -JJ and one normal JJ (or 0 -JJ) structures [21]. $0-\pi$ qubits can be implemented in different ways. Recently, an intrinsically error-protected superconducting $0-\pi$ qubit with a long decoherence time (1.6 ms) has been experimentally realized [22].

Thus, both the superconducting systems, Co and CoSi_2 , have potential applications in quantum technology. With the possibility of localized pulsed laser annealing of a Co film on Si to form CoSi_2 [23], realization of devices incorporating functionalities of both the superconductors – Co and CoSi_2 , on the same Si substrate can be envisaged.

In this article, we explore the conversion of one superconducting system (Co) to another superconductor (CoSi_2), achieved via annealing and compare their superconducting properties with a view to utilize the latter in superconducting quantum circuits.

2. Experimental methods

Co films were deposited using electron beam evaporation onto a (100)-oriented n-type Si substrate (resistivity $\sim 3 - 8.5 \Omega\cdot\text{cm}$) at room temperature under high vacuum. Prior to deposition, the Si substrate was cleaned in 1% aq. HF solution to etch-off the native oxide (SiO_x) layer. Earlier investigations have shown that this method of growth produces polycrystalline Co films, which are also superconducting [14, 15]. To investigate the superconductivity in the Co film, electrical resistivity measurements were performed using conventional linear four-probe technique (with indium-silver solder contacts) under externally applied magnetic fields inside a commercial physical property measurement system (PPMS of M/s. Quantum Design) down to low temperature (2 K). To apply magnetic fields along different directions with respect to the film (sample) plane, the sample was rotated using a rotator-puck/sample-insert provided with the PPMS. This has allowed us to measure critical field anisotropy, which was not investigated in earlier studies [14].

Following that, the superconducting Co film was converted into a superconducting CoSi_2 film via annealing at 850 °C under high vacuum (HV) conditions ($< 5 \times 10^{-6}$ mbar) for 1.5 hours. To investigate the superconductivity of the CoSi_2 film, resistivity measurements were carried out using van der Pauw (vdP) technique inside a dilution refrigerator that could cool down to 30 millikelvin. The contact pads for the vdP configuration were prepared by thermal evaporation of Ti/Au, patterned by lift-off photolithography. The magnetic field could only be applied in the out-of-plane direction with the available sample space configuration inside the dilution refrigerator.

X-ray characterizations of both the Co film and the CoSi_2 film were done at room temperature in a Rigaku SmartLab diffractometer with Cu-K_α x-rays ($\lambda = 1.5406 \text{ \AA}$). X-ray reflectivity (XRR) was performed on the Co film to determine its thickness, roughness and electron density distribution (layer structure), while grazing incidence x-ray diffraction (GIXRD) was performed on both the Co and the CoSi_2 films to identify their phases. Moreover, cross-sectional high resolution transmission electron microscopy (HRTEM) was performed on the CoSi_2 film to investigate the thickness and crystal orientation of the film with respect to the substrate.

3. Results and Discussions

3.1. Cobalt film

3.1.1. Characterization

Figure 1 (a) shows GIXRD of the film, indicating the (0002) peak of Co. This indicates that the hcp phase of normal Co dominates the film. On the other hand, in order to get the information of the overall film stack (*i.e.*, thickness, individual layer densities, surface and interfacial roughness), XRR data were carefully analyzed, since it can reveal the electron scattering length density (ESLD) or electron density depth profile (proportional to mass density depth profile) with very high depth resolution ($\sim 1 \text{ \AA}$), and rms roughness parameters in the direction normal to the film plane. We obtained a total thickness of $30.89(3) \text{ nm}$ for the Co film from the XRR measurement. The best fit to the XRR data ($\chi^2 = 1.17 \times 10^{-2}$), as shown by solid orange-colored line in Fig. 1(b), was obtained by considering a ESLD profile that shows higher ESLDs at the Co/Si interface as well as near

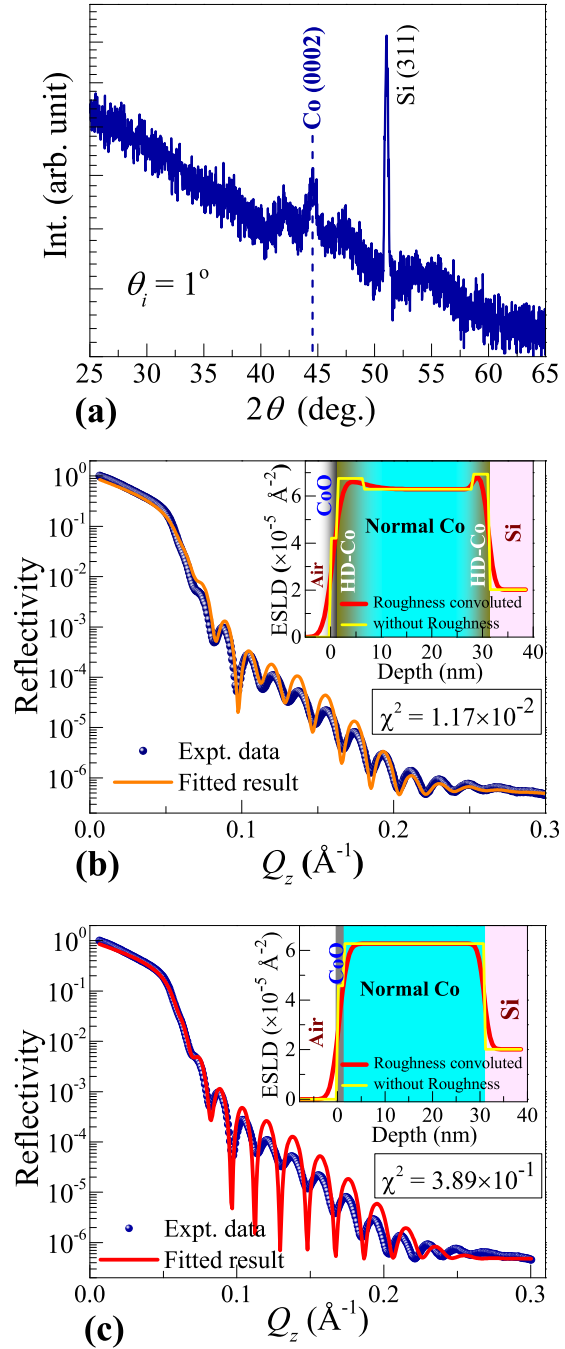


Figure 1. (a) GIXRD pattern (at incident angle, $\theta_i = 1^\circ$) of the Co film. The extra peak from the substrate was identified from ϕ -scan measurement. (b) XRR of the Co film fitted with the tri-layer model as described in the text. (c) XRR of the same film fitted with Si/Normal-CO/CoO layer model, which shows relatively mediocre fit as compared to that in (b). Insets of both the panels show the ESLD profile corresponding to the XRR fits.

Table 1. Depth dependent parameters of Co film extracted from XRR measurement:

Layer	Thickness (nm)	ESLD ($\times 10^{-5} \text{\AA}^{-2}$)	Roughness (nm)
CoO	1.27(9)	4.53(7)	1.4(6)
HD-Co	1.61(7)	6.87(1)	1.2(9)
Normal Co	24.47(2)	6.27(3)	1.0(0)
HD-Co	3.52(5)	6.70(5)	0.5(5)
Si substrate	—	2.01(5)	1.0(3)

the Co/CoO interface (shown in the inset of the the panel) [A CoO layer (~ 2 nm) naturally grows on the Co film after removing it from the vacuum chamber following film deposition]. This kind of hybrid three-layer structure – HDNM-Co/Normal-Co/HDNM-Co – forms in a self-organised manner, similar to those reported in Ref. [15, 16]. The method of detailed analysis may be found in Refs. [15, 16]. The ESLD, thickness and roughness parameters obtained from XRR of the present sample are given in Table 1. In our case, we obtained a layer of $\text{ESLD} = 6.87(0) \times 10^{-5} \text{\AA}^{-2}$ (of thickness 1.27(9) nm) close to the Co/CoO interface and another layer of $\text{ESLD} = 6.70(5) \times 10^{-5} \text{\AA}^{-2}$ (of thickness 3.52(5) nm) at the Co/Si interface, both of which are higher in density compared to that of Normal-Co layer (of thickness 24.47(2) nm) in the middle. [For comparison, we show that the XRR data could not be fitted properly assuming a single uniform density Normal Co layer ($\text{ESLD} = 6.27(3) \times 10^{-5} \text{\AA}^{-2}$) (with obvious CoO layer on top) along the whole depth of the film, as shown in Fig. 1 (c)]. Such HDNM Co layers in the obtained tri-layer structure are non-magnetic with nanoscale grains [15, 16] and show inhomogeneous superconductivity as reported in Ref. [14]. Since the nature of superconductivity was reported to be inhomogeneous in nature, this stimulated us to investigate the superconducting behavior

with variation of direction of magnetic field, as described below.

3.1.2. Transport properties

To investigate the nature of superconductivity, we measure the temperature variation of resistance (down to $T = 2$ K only) under various magnetic field strengths applied parallel (IP) and perpendicular (OOP) to the film plane. The results are presented in Fig. 2(a) and (b). We observe that the superconductivity is remarkably suppressed by a magnetic field of ~ 2 T and ~ 0.5 T applied IP and OOP, respectively.

However, one of the important features of these resistance (R) vs temperature (T) (or $R - T$) curves is the non-vanishing resistance in the superconducting state (*i.e.*, below T_c , even in the absence of magnetic field). There can be three possible contributions to this non-zero resistance: (i) due to presence of a comparatively higher resistive CoO layer at the top; (ii) due to contact resistance of the probes and sensitivity of the measuring instruments [24]; or (iii) due to granular nature of the sample itself [25, 26]. Moreover, our sample has superconducting Co layers in the background of a normal Co layer. In our sample, there is only 4% drop in resistance in the superconducting state with respect to the normal state. This can be explained considering the resistance contribution from the CoO layer and the normal Co layer [schematically shown in Fig. 2(c)], even if we neglect the contact resistance. It should be noted that the non-zero resistance in the superconducting state of granular metals might also be attributed to Josephson coupling between an increasing number of pairs of grains with decreasing temperature [25, 26, 27, 28]. By virtue of competition between the Josephson coupling energy (E_J) and capacitive

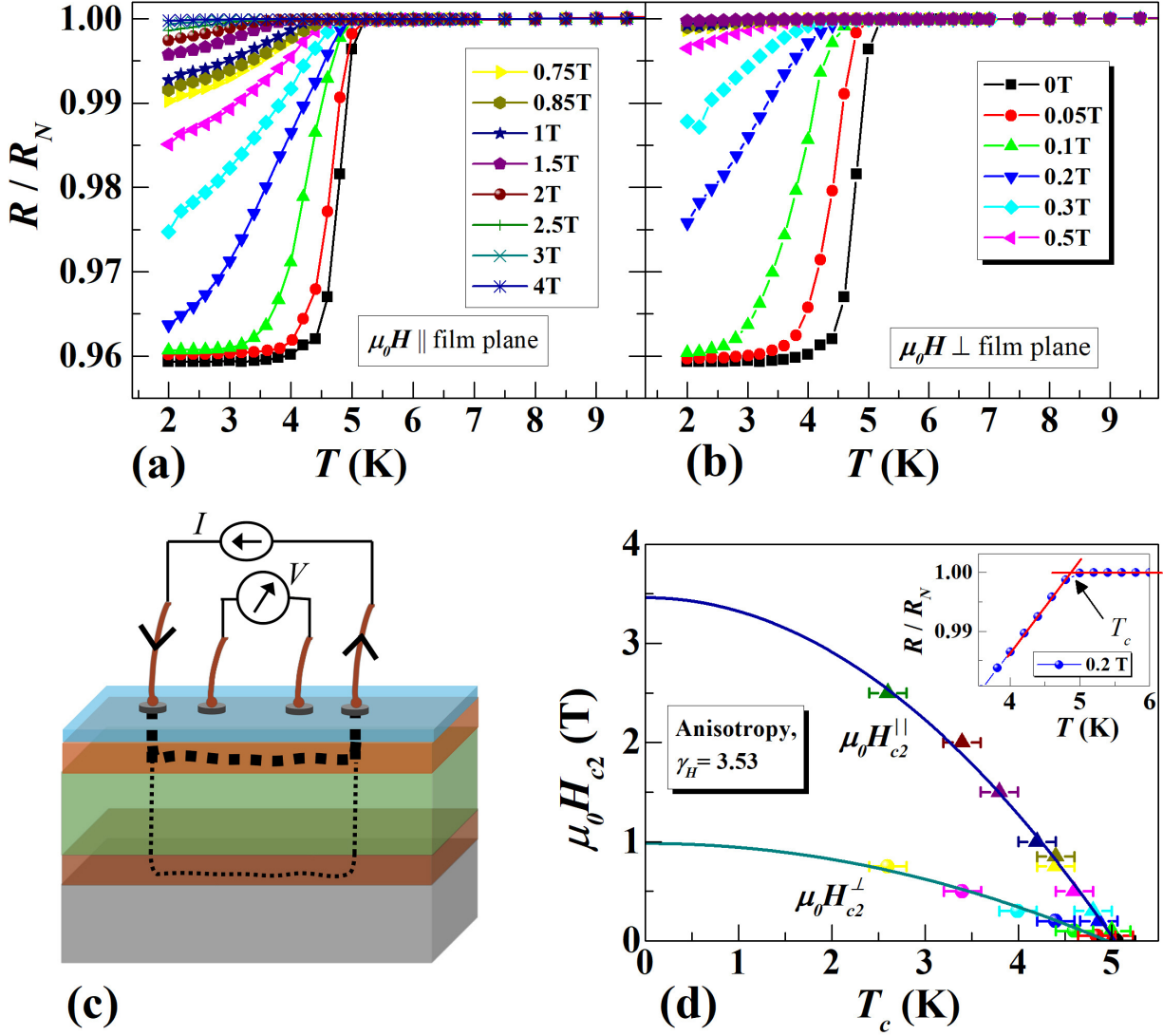


Figure 2. $R - T$ variation of the Co film at various magnetic fields applied: (a) along the film plane (in-plane/IP); (b) perpendicular to the film plane (out-of-plane/OOP). (c) Schematic of the linear four-probe measurement setup. (d) $\mu_0 H_{c2} - T_c$ phase diagram of the film showing clear anisotropy in the upper critical fields (Symbols: Data obtained from experimental $R - T$ curves, Solid lines: Fit using BCS model). Inset shows how we defined the T_c , marked by the arrow.

coupling energy (E_c) between the grains, the superconducting state appears when $E_J \gg E_c$.

To generate the $\mu_0 H_{c2} - T_c$ phase diagram, we first define the critical temperature (T_c) as the temperature where superconductivity sets in (onset of superconductivity) (as shown in the inset of Fig. 2(d) with an arrow). Thus we generate the phase diagram from the $R - T$

plots as shown in the main panel of Fig. 2(d), which reveals a clear anisotropy in the upper critical field along the two directions. We determine these upper critical fields namely $\mu_0 H_{c2}^{\parallel}(0)$ and $\mu_0 H_{c2}^{\perp}(0)$ from fitting, using the BCS model:

$$\mu_0 H_{c2} = \mu_0 H_{c2}(0) \left[1 - \left(\frac{T}{T_{c0}} \right)^2 \right] \quad (1)$$

where $\mu_0 H_{c2}(0)$ is the zero temperature upper

Table 2. Parameters extracted from the BCS fit to the $\mu_0 H_c - T_c$ phase diagram:

Field Direction	$\mu_0 H_{c2}(0)$ (T)	$T_c(0)$ (K)	γ_H	ξ_0 (nm)
IP ($\mu_0 H_{c2}^{\parallel}$)	3.46(6)	5.03(1)	3.53	9.75(3)
OOP ($\mu_0 H_{c2}^{\perp}$)	0.98(4)	4.94(5)		18.32(2)

critical field and T_{c0} is the absolute critical temperature. We also define the anisotropy in the upper critical field as:

$$\gamma_H = \frac{\mu_0 H_{c2}^{\parallel}(0)}{\mu_0 H_{c2}^{\perp}(0)} \quad (2)$$

The obtained values are summarized in Table 2. In comparison to robust 2D superconducting systems where anisotropy is quite strong ($\gamma_H \sim 10$), the anisotropy of our system ($\gamma_H \approx 3.5$) indicates a quasi-2D nature of superconductivity in it. We have layered superconducting regions (or grains) of HDNM Co whose aspect ratio of lateral dimension (≈ 10 nm) to thickness (≈ 3 nm) [15] is almost 3. Therefore it is expected that the coherence length along the film-normal is longer than that along the film-plane, which induces an anisotropic pair-breaking mechanism depending on the direction of the magnetic field applied to the film. This explains anisotropy in the upper critical fields.

In case of the orbital-limiting effect, which is dominant under perpendicular (OOP) magnetic fields, Cooper pair breaking is induced by the momentum, $e\vec{A}/\hbar c$, where \vec{A} is the vector potential, and eventually, the kinetic energy of supercurrent exceeds the superconducting gap energy [29, 30]. Thus, the upper critical field is recognized as the orbital-limiting field, $\mu_0 H_{orb} = \phi_0/(2\pi\xi^2)$, which depends on the coherence length of Cooper pair, ξ . Here ϕ_0 is the magnetic flux quantum.

On the other hand, for a 2D weak coupling BCS superconductor, the upper critical

field becomes limited by the so called Pauli paramagnetic limit (or the Chandrasekhar-Clogston limit) [31, 32], where the Zeeman splitting energy of individual electron spin exceeds the superconducting energy gap and thus Cooper pair becomes energetically unstable. This Pauli limiting field becomes important under parallel (IP) magnetic fields and is given by $\mu_0 H_P \approx \frac{1.76k_B T_c}{\sqrt{2}\mu_B}$, where k_B and μ_B are the Boltzmann's constant and Bohr magneton, respectively. Taking $T_c = 5$ K, we have $\mu_0 H_P = 9.2$ T, which is way larger than the $\mu_0 H_{c2}^{\parallel}(0)$ of our Co film suggesting a very weak coupling regime of superconductivity.

3.2. CoSi₂ film

We now turn towards the CoSi₂ film formed by annealing of the Co / Si thin film system discussed so far.

3.2.1. Characterization

Figure 3 shows the GIXRD pattern of the annealed sample. The peaks at 28.84°, 48.12° and 57.18° correspond to the (111), (220), and (311) orientations of CoSi₂ and confirm that

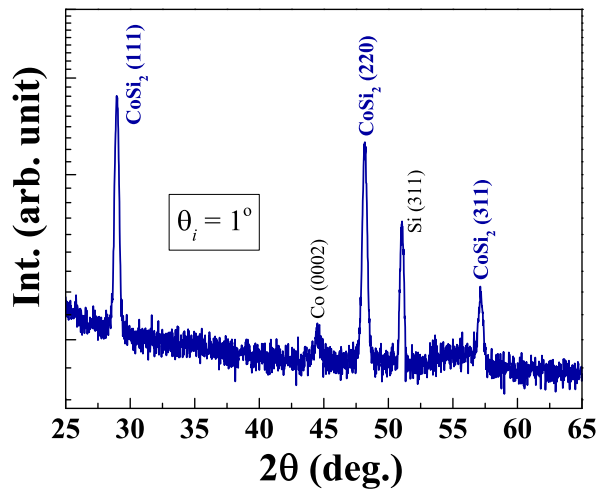


Figure 3. GIXRD pattern (at incident angle, $\theta_i = 1^\circ$) of the CoSi₂ film. The extra peak from the substrate was identified from ϕ -scan measurement.

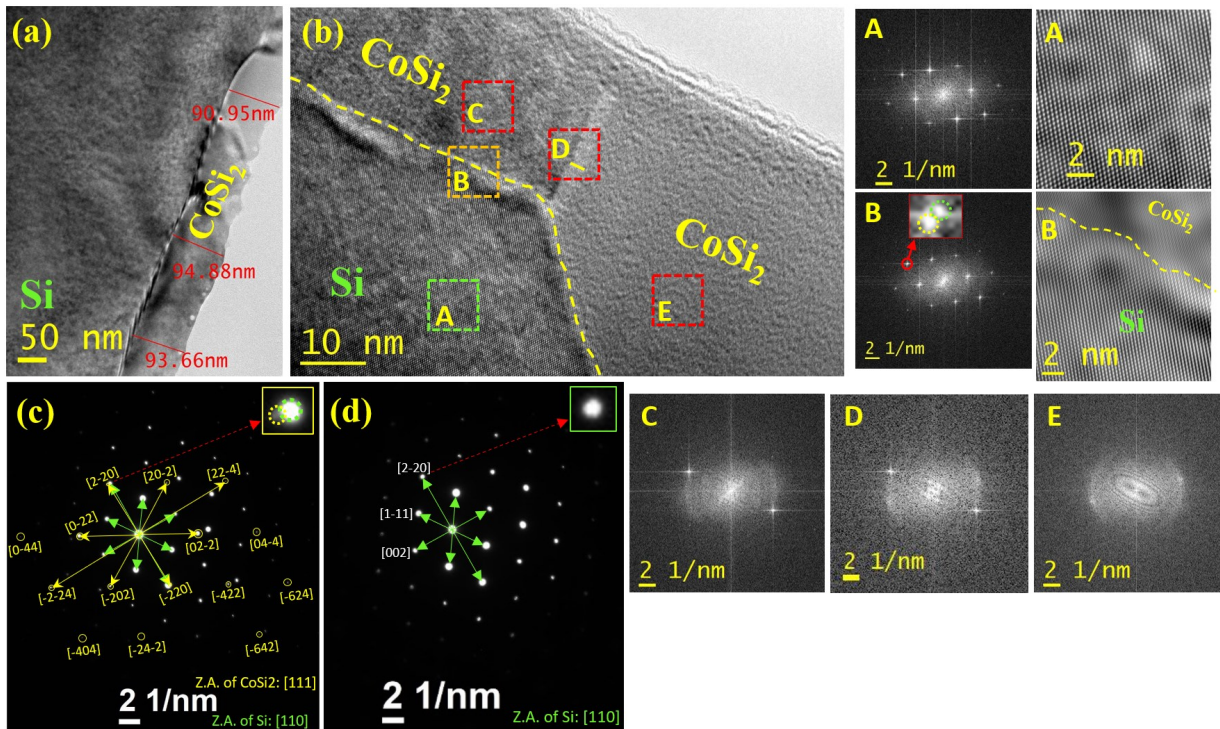


Figure 4. (a) Cross-sectional TEM image of the Si/CoSi₂ sample at low magnification. The average thickness of CoSi₂ is around 90 nm. (b) HRTEM image showing two different grains within the CoSi₂ film. FFT is performed on the regions marked A to E. The FFT image in B (substrate/film interface) shows splitting of the spot due to different crystal orientation of CoSi₂ with respect to the Si substrate. Also, the different orientation of the two grains of CoSi₂ is clear from the corresponding FFT images as we gradually go from region C, D (grain boundary region) to E. (c) SAED patterns of CoSi₂ film + Si substrate, showing splitting of the marked [2̄2̄0] spot (magnified in the top corner of the same image). (d) SAED pattern of the Si substrate only, showing a single spot at the [2̄2̄0] position. Note that the images were collected by setting zone-axis (Z.A.) parallel to [110] direction of Si. Analysis of the SAED patterns reveal that Z.A. of CoSi₂ is parallel its (111) direction, which means, orientation of CoSi₂ is such that (111) planes of CoSi₂ is parallel to (110) planes of Si.

the CoSi₂ phase has already formed with 1.5 hours of annealing at 850 °C and manifest good crystallinity of the film. To get further information about the crystalline nature of the film, the cross-sectional HRTEM of the film has been performed, as shown in Fig. 4(a)-(d). From the low magnification image [Fig. 4(a)], the overall film thickness is found to be around 90 nm. The high magnification HRTEM image in Fig. 4(b) further confirms that the film has multiple CoSi₂ grains. The relative orientation of the CoSi₂ film with respect to the Si substrate can be visualised from the SAED pattern in figure panel (c). For comparison

the SAED pattern of the Si substrate is shown in panel (d). In this film, (111) planes of CoSi₂ is parallel to (110) planes of Si. To get further insight into the detailed crystallinity, the fast Fourier transform (FFT) has been performed in various regions as marked by (A) to (E) of the image in Fig. 4(b) and are shown in the corresponding sub-panels. It is interesting to note the changes in the FFT diffraction patterns as we go from one grain to the other across the grain boundary [sub-panels (C) to (E)]. This confirms the different orientations of the two grains separated by the grain boundary. It should be noted that

two such superconducting grains, separated by a grain boundary, can behave as an inherent Josephson junction, the effects of which can be seen in the resistivity and $I-V$ characteristics of the sample.

3.2.2. Transport Properties

A. Resistivity

The temperature dependence of the resistance ($R - T$) of the CoSi₂ film measured in van-der Pauw technique for two different currents under zero magnetic field is presented in Fig. 5 (a). Firstly, we observe a superconducting transition around 900 mK with a prominent peak near the transition temperature. Secondly, although there is almost an order of magnitude drop in resistance in the superconducting state with respect to the normal state, the resistance value in the superconducting state is still non-zero. This again hints towards the Josephson coupling between the superconducting grains, which we will discuss later.

The peak in the resistive transition is easily reproduced by considering simultaneously the inhomogeneity of the sample and the geometry of the electrical probes. Assuming a simple equivalent circuit representation with normal state resistances R_1 , R_2 , R_3 , and R_4 between each couple of probes in the vdP configuration as in Fig. 6(a), the measured resistance $R_{meas} = V_{measured}/I_{input}$ is given by [33, 34]

$$R_{meas} = \frac{R_1 \times R_3}{\sum_i R_i} \quad (3)$$

Because of the inhomogeneity of our sample, the four resistors can have different T_c . For simplicity, we further assume that $R_1 = R_3$ and $R_2 = R_4$ at all temperatures. Then, using Eq.3 we fit the zero-magnetic-field $R-T$ curve as shown in Fig. 6(b).

Similar to the $R - T$ curve in Fig. 5 (a), we notice a peak in resistance near the critical magnetic field in the $R - \mu_0 H$ curve in Fig. 5 (b). In order to explain this behaviour, it is reasonable to argue that two zones having different T_c , as described in previous paragraph, are also characterized by different critical magnetic fields. To fit the $R-T$ and $R-\mu_0 H$ curve we justify our arguments as follows:

- (i) The regions with higher normal state resistance (R_N) behave as more inhomogeneous region with lower T_c and lower $\mu_0 H_c$; and conversely the regions with low R_N will have higher T_c and higher $\mu_0 H_c$ [33, 26],
- (ii) Apart from the measure of R_N , the degree of inhomogeneity can be evaluated qualitatively from the width of the transition: a higher inhomogeneity implies a wider transition [35].

Considering the above arguments, we first fit the zero field $R - T$ curve by taking $T_c^{R_2} = 0.95 \text{ K} > T_c^{R_1} = 0.9 \text{ K}$. Accordingly, we relate the slight T_c difference of $\approx 50 \text{ mK}$ to the presence of inhomogeneity/disorder [36], and thus have $\mu_0 H_c^{R_2} > \mu_0 H_c^{R_1}$, where $\mu_0 H_c^{R_{1(2)}}$ is the critical magnetic field of the zone described by the resistor $R_{1(2)}$. Using this argument, we fit the $R - H$ curve at zero temperature [see Fig. 6(c)]. From these fits, we note that the two T_c 's are located one at the peak point of the experimental curve and the other at the point where the normal state resistance is just reached. Utilizing this observation, we extract the pair of values of $\mu_0 H_c$ at different temperatures from the experimental $R - H$ curves and generate the $\mu_0 H_c - T_c$ phase diagram as shown in Fig. 6(d). We further note that the phase diagram does not present a sharp boundary between the normal and superconducting state, rather a broad region (shaded area in the figure), where the experimentally extracted values represent the

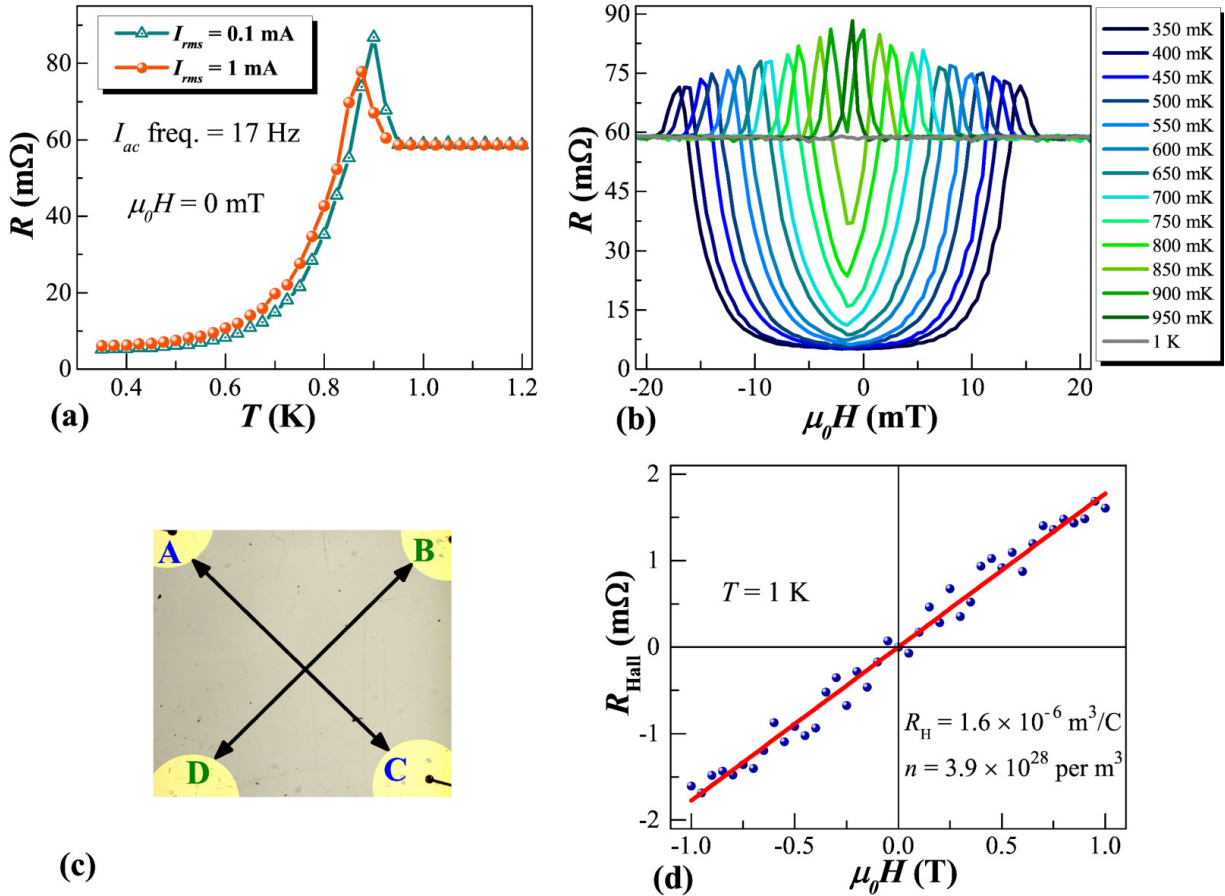


Figure 5. (a) $R - T$ behavior of the CoSi_2 film (with a peak near the transition temperature) measured at two different currents at $\mu_0 H = 0$ T. (b) Magnetic field variation of resistance ($R - \mu_0 H$) of the film measured at various temperatures ranging from 350 mK to 1 K with 0.1 mA current. (c) Optical microscope image of the sample with contact pads in van der Pauw geometry. [The current and voltage probes were connected mutually perpendicular to each other (along the diagonal) as marked by arrows for Hall effect measurement]. (d) Normal state Hall resistance of the CoSi_2 film measured at $T = 1$ K. The carrier density (n) and Hall coefficient (R_H) are mentioned inside the figure for convenience.

two limits of the phase boundary. We then fit the $\mu_0 H_c - T_c$ data using the BCS model (as in Eq. 1) and find the highest critical field $\mu_0 H_c(0) \approx 20$ mT, comparable to previous results on CoSi_2 films [37, 38].

We also measured the Hall effect in the CoSi_2 film at normal state ($T = 1$ K) as shown in Fig. 5(c) and (d), which indicates that the charge carriers are holes, in consistency with previous results [5, 39]. We found the Hall coefficient $R_H = 1.6 \times 10^{-6} \text{ m}^3/\text{C}$, hole concentration $n = 3.9 \times 10^{28} \text{ m}^{-3}$ and a

Hall mobility $\mu_H = 1.18 \text{ T}^{-1}$. From this, we estimated the Fermi wave vector $k_F [= (3\pi^2 n)^{1/3}] \approx 1.05 \times 10^{10} \text{ m}^{-1}$ and a Fermi velocity of $v_F \approx 1.22 \times 10^6 \text{ m/s}$ [5, 40, 41]. We further calculated the mean free path, $l = 6.12 \times 10^{-10} \text{ m}$ from the longitudinal resistivity (ρ) using the relation: $l = 3\pi^2 \hbar / (k_F^2 e^2 \rho)$, and estimated the disorder factor $k_F l \approx 6.43$. Accordingly, the high value of $R_H = 1.6 \times 10^{-6} \text{ m}^3/\text{C}$ in our CoSi_2 film is consistent with the low value of $k_F l$ in comparison with recent reports on polycrystalline CoSi_2 film [39].

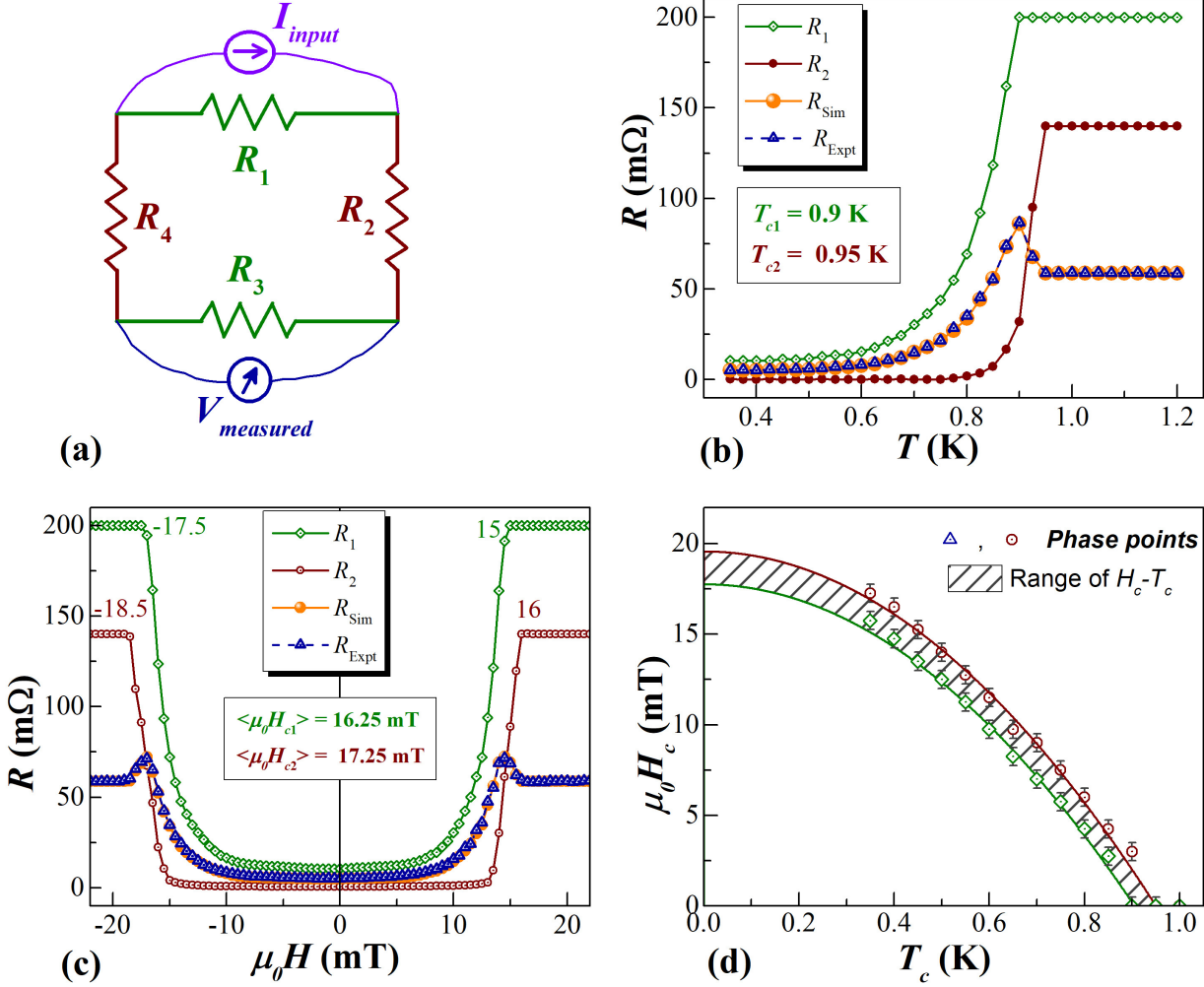


Figure 6. (a) Schematic of effective resistance model to account for the peak near the superconducting transition. Simulation using the effective two-resistance model of – (b) experimental $R - T$ data at zero field, and (c) experimental $R - \mu_0 H$ data at 350 mK. (d) $\mu_0 H_c - T_c$ phase diagram generated from the experimentally measured $R - H$ curves, obtained using the effective two-resistance model. The solid lines indicate fitting using the BCS model. The shaded portion shows the broadened phase boundary between the normal and the superconducting state of the total film.

B. $I - V$ characteristics

To find the critical current (I_c), we measured the $I - V$ characteristics of the CoSi₂ film at various temperatures under zero magnetic field, as shown in Fig. 7(a). Instead of a sharp transition to a normal state (recognised by linear region), we observe exponential type of behaviour, which probably is due to presence of inhomogeneity [42, 43]. The linear region above a certain (critical) current indicates the normal state region. Interestingly we

also observe a peculiar hump near the critical current. By considering the equivalent resistor circuit as in Fig. 6(a), we can argue that the hump in $I - V$ characteristics occurs due to two different critical currents of the two different resistive regions [34] (R_1 and R_2) as shown in Fig. 7(b) (left axis). The critical currents can be best extracted from the dV/dI vs I curves as shown in Fig. 7(b) (right axis). From each $I - V$ curves in Fig. 7(a), we determine the corresponding I_{c1} and I_{c2} values and thus

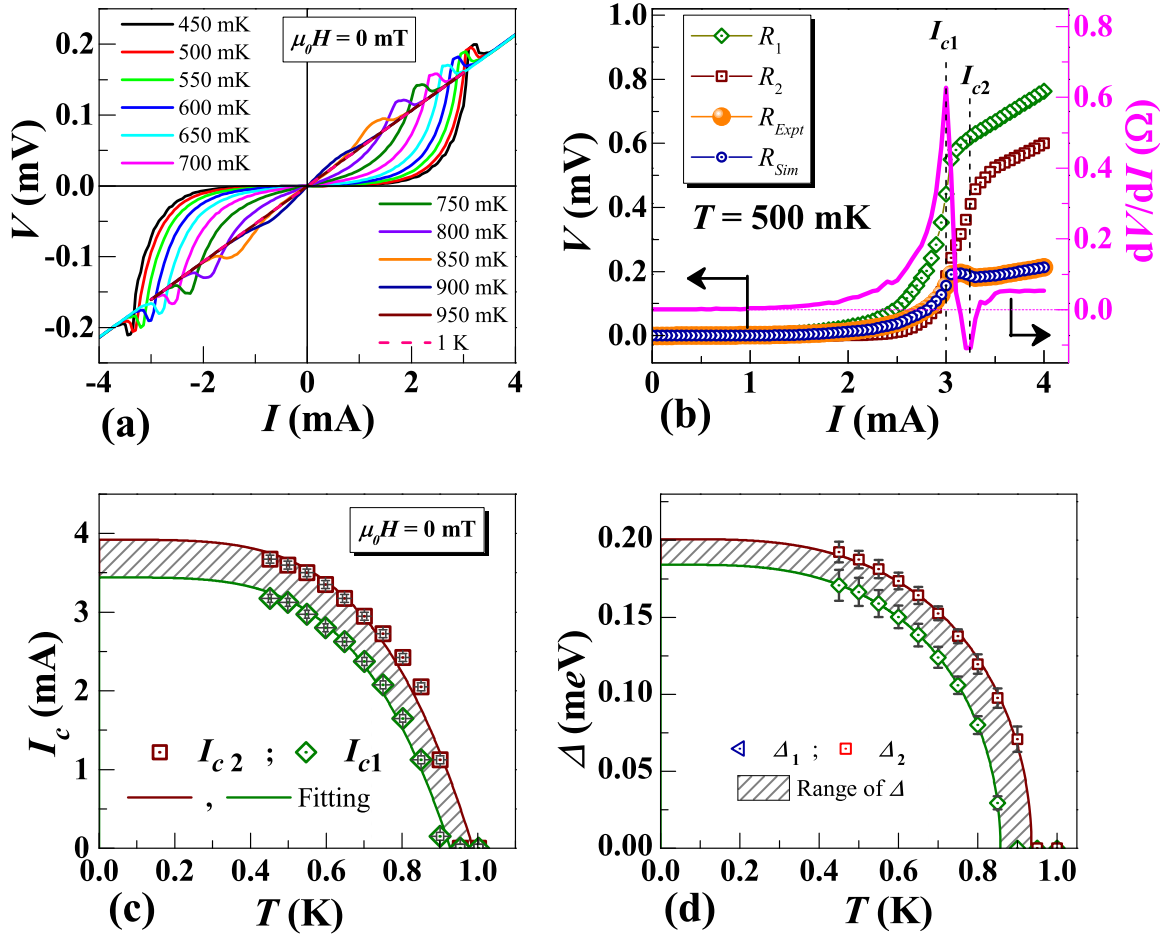


Figure 7. (a) $I - V$ characteristic of the CoSi₂ film measured at various temperatures at zero magnetic field. (b) As an example, $I - V$ at 500 mK is fitted using the two-resistance model that justifies the hump in the $I - V$ curves. The corresponding critical currents I_{c1} and I_{c2} can be obtained from the dV/dI curves as shown (right axis). (c) $I_c - T$ phase diagram generated from the experimentally measured $I - V$ curves. (d) Δ vs T phase diagram, where values of Δ at each temperature is estimated from the $I - V$ curves. Solid lines are fitting using simplified BCS model (see main text). The shaded portions in both panels (c) and (d) indicate the broadened phase boundary between the normal and the superconducting state of the total film.

generate the $I_c - T$ phase diagram at zero magnetic field, as shown in Fig. 7(c). From the $I - V$ characteristics in Fig. 7(a), for each temperature, we also estimate the values of Δ_1 and Δ_2 (in meV units) (where $2\Delta = E_g$, the energy gap) by taking the voltage values corresponding to I_{c1} and I_{c2} and generate the $\Delta - T$ phase diagram which is shown in Fig. 7(d).

Next, in order to speculate the possibility of internal Josephson coupling from the $I_c - T$

curve, we take into account the Ambegaokar-Baratoff (AB) relation [42, 44]:

$$I_c(T) = I_c(0) \times \frac{\Delta(T)}{\Delta(0)} \times \tanh\left(\frac{\Delta(T)}{2k_B T}\right) \quad (4)$$

where $\Delta(T)$ is the temperature dependent energy gap. In order to do so, we first estimate the zero temperature energy gap, $\Delta(0)$, for each region by fitting the $\Delta(T)$ vs T curves (Fig. 7d) using an approximate formula that

reproduces well the BCS behavior [42]:

$$\Delta_i(T) = \Delta_i(0) \left[1 - \frac{1}{3} \left(\frac{T}{T_c^i} \right)^4 \right] \sqrt{1 - \left(\frac{T}{T_c^i} \right)^4} \quad (5)$$

We obtained $\Delta_1(0) = 0.185(2)$ meV and $\Delta_2(0) = 0.199(3)$ meV; however, these are somewhat higher when compared with $\Delta(0)$ values calculated using the BCS prediction [45, 46]: $\Delta(0) = 1.76k_B T_c$ for clean systems. This kind of situations have been encountered earlier due to the presence of inhomogeneity [47, 48]. Nonetheless, utilizing these in Equation 4, we fit the $I_c - T$ curve to obtain the zero temperature critical currents $I_{c1}(0) = 3.44(6)$ mA and $I_{c2}(0) = 3.93(9)$ mA. The fitting of the $I_c - T$ curves with Ambegaokar-Baratoff formula indicates the possibility of the presence of weak Josephson coupling between the polycrystalline regions, and is still under our scrutiny.

4. Conclusion

We have presented the conversion of one superconducting system (self-organized HDNM Cobalt film on Si) into another (CoSi₂ film) by annealing the former under vacuum and compared their superconducting properties. The HDNM Co film, which had $T_c \approx 5$ K showed anisotropy in the upper critical field with respect to its in-plane and out-of-plane directions, comparable to the HDNM Co grain dimensions. CoSi₂ films showed T_c around 0.9 K – somewhat less compared to its epitaxial form. However, the critical current densities and upper critical fields were comparable with its previously reported results. Measurement performed in van-der Pauw geometry revealed some distinctive features near the transition temperature (also field and current) which were explained considering multiple-resistance model for polycrystalline regions (confirmed by

HRTEM) of varying superconducting properties. Analysis of the critical current and energy gap parameter revealed possible presence of Josephson coupling between the polycrystalline CoSi₂ regions. Superconducting materials with internal Josephson junctions, *e.g.*, disordered superconductors or granular superconductors can have high kinetic inductance. While normal aluminium is commonly used for fabricating transmon qubits, granular aluminium superconductors, with their high kinetic inductance, are used in fabricating fluxonium qubits [49, 50], desirable for building quantum annealing computers. While the Co thin film superconductor is a disordered superconductor, recent studies suggest that CoSi₂ is a valuable addition to the toolkit of materials for quantum circuit fabrication [51].

We further aim to develop both polycrystalline and epitaxial CoSi₂ films by annealing such trilayer structured Co films, for fabricating superconducting quantum circuits in the near future. CoSi₂, being resistant to oxidation, may also be valuable for the suppression of undesirable two-level-systems.

Acknowledgments

S.M, B.B and B.N.D acknowledge TCG CREST for funding. S.M and B.B also acknowledge help from Prof. Biswajit Karmakar of SINP during measurement in dilution refrigerator and Mr. Arnab Bhattacharya and Mr. Afsar Ahmed of SINP during measurement in PPMS.

References

- [1] Kjaergaard M, Schwartz M E, Braumüller J, Krantz P, Wang J I J, Gustavsson S and Oliver W D 2020 *Annu. Rev. Condens. Matter Phys.* **11** 369–395

- [2] Lau J W Z, Lim K H, Shrotriya H and Kwek L C 2022 *AAPPS Bulletin* **32** 27
- [3] Nakamura Y, Pashkin Y A and Tsai J 1999 *Nature* **398** 786–788
- [4] Siddiqi I 2021 *Nat. Rev. Mater.* **6** 875–891
- [5] Chiu S P, Yeh S S, Chiou C J, Chou Y C, Lin J J and Tsuei C C 2017 *ACS Nano* **11** 516–525
- [6] Zhang S L and Östling M 2003 *Crit. Rev. Solid State Mater. Sci.* **28** 1–129
- [7] Furukawa S and Ishiwarara H 1983 *Jpn. J. Appl. Phys.* **22** 21
- [8] Shi J, Irie T, Takahashi F and Hashimoto M 2000 *Thin Solid Films* **375** 37–41
- [9] Mahato J C, Das D, Juluri R R, Batabyal R, Roy A, Satyam P V and Dev B N 2012 *Appl. Phys. Lett.* **100**
- [10] Tung R, Bean J, Gibson J, Poate J and Jacobson D 1982 *Appl. Phys. Lett.* **40** 684–686
- [11] Tsutsumi K, Takayanagi S and Hirano T 1997 *Physica B* **237** 310–311
- [12] Kittel C and McEuen P 2018 *Introduction to Solid State Physics* 8th ed (John Wiley & Sons) ISBN 9780471415268, 047141526X, 0471680575
- [13] Shimizu K, Kimura T, Furomoto S, Takeda K, Kontani K, Onuki Y and Amaya K 2001 *Nature* **412** 316–318
- [14] Banu N, Aslam M, Paul A, Banik S, Das S, Datta S, Roy A, Das I, Sheet G, Waghmare U *et al.* 2020 *Europhys. Lett.* **131** 47001 ; 2017 *arXiv preprint arXiv:1710.06114*
- [15] Banu N, Singh S, Satpati B, Roy A, Basu S, Chakraborty P, Movva H C, Lauter V and Dev B 2017 *Sci. Rep.* **7** 1–8
- [16] Banu N, Singh S, Basu S, Roy A, Movva H C, Lauter V, Satpati B and Dev B 2018 *Nanotechnology* **29** 195703
- [17] Yoo C, Cynn H, Söderlind P and Iota V 2000 *Phys. Rev. Lett.* **84** 4132
- [18] Baek B, Rippard W H, Benz S P, Russek S E and Dresselhaus P D 2014 *Nat. Commun.* **5** 3888
- [19] Bhatia E and Senapati K 2022 *Supercond. Sci. Technol.* **35** 094004
- [20] Pompeo N, Torokhtii K, Cirillo C, Samokhvalov A, Ilyina E, Attanasio C, Buzdin A I and Silva E 2014 *Phys. Rev. B* **90** 064510
- [21] Yamashita T, Tanikawa K, Takahashi S and Maekawa S 2005 *Phys. Rev. Lett.* **95** 097001
- [22] Gyenis A, Mundada P S, Di Paolo A, Hazard T M, You X, Schuster D I, Koch J, Blais A and Houck A A 2021 *PRX Quantum* **2** 010339
- [23] Lee P S, Pey K L, Chow F, Tang L, Tung C H, Wang X and Lim G 2006 *IEEE Electron Device Letters* **27** 237–239
- [24] Buckel W and Kleiner R 2008 *Superconductivity: fundamentals and applications* (John Wiley & Sons)
- [25] Adkins C, Thomas J and Young M 1980 *J. Phys. C: Solid State Phys.* **13** 3427
- [26] Durkin M, Garrido-Menacho R, Gopalakrishnan S, Jaggi N K, Kwon J H, Zuo J M and Mason N 2020 *Phys. Rev. B* **101** 035409
- [27] Abeles B 1977 *Phys. Rev. B* **15** 2828
- [28] Dynes R, Garno J and Rowell J 1978 *Phys. Rev. Lett.* **40** 479
- [29] Helfand E and Werthamer N 1966 *Phys. Rev.* **147** 288
- [30] Werthamer N, Helfand E and Hohenberg P 1966 *Phys. Rev.* **147** 295
- [31] Chandrasekhar B 1962 *Appl. Phys. Lett.* **1** 7–8
- [32] Clogston A M 1962 *Phys. Rev. Lett.* **9** 266
- [33] Vaglio R, Attanasio C, Maritato L and Ruosi A 1993 *Phys. Rev. B* **47** 15302
- [34] Park M, Isaacson M and Parpia J 1997 *Phys. Rev. B.* **55** 9067
- [35] Benfatto L, Castellani C and Giamarchi T 2009 *Phys. Rev. B* **80** 214506
- [36] Kim J J, Kim J, Shin H J, Lee H J, Lee S, Park K W and Lee E H 1994 *J. Phys.: Condens. Matter* **6** 7055
- [37] Chiu S P, Tsuei C, Yeh S S, Zhang F C, Kirchner S and Lin J J 2021 *Sci. Adv.* **7** eabg6569
- [38] Badoz P, Briggs A, Rosencher E and d’Avtaya F A 1985 *J. Physique Lett.* **46** 979–983
- [39] Heredia E A, Chiu S P, Nguyen B A V, Wang R T, Wu C Y, Yeh S S and Lin J J 2024 *Phys. Rev. B* **110** 024201
- [40] Radermacher K, Monroe D, White A E, Short K T and Jevasinski R 1993 *Phys. Rev. B* **48** 8002
- [41] Krontiras C, Salmi J, Grönberg L, Suni I, Heleskivi J and Rissanen A 1985 *Thin Solid Films* **125** 93–99
- [42] Venditti G, Biscaras J, Hurand S, Bergeal N, Lesueur J, Dogra A, Budhani R, Mondal M, Jesudasan J, Raychaudhuri P *et al.* 2019 *Phys. Rev. B* **100** 064506
- [43] Veyrat A, Labracherie V, Bashlakov D L, Cagliaris F, Facio J I, Shipunov G, Charvin T, Acharya R, Naidyuk Y, Giraud R *et al.* 2023 *Nano Letters* **23** 1229–1235
- [44] Ambegaokar V and Baratoff A 1963 *Phys. Rev. Lett.* **10** 486
- [45] Tinkham M 2004 *Introduction to Superconductiv-*

ity vol 1 (Dover, Mineola (New York))

- [46] Bardeen J, Cooper L N and Schrieffer J R 1957 *Phys. Rev.* **108** 1175
- [47] Giaever I and Megerle K 1961 *Phys. Rev.* **122** 1101
- [48] Douglass Jr D and Meservey R 1964 *Phys. Rev.* **135** A19
- [49] Grünhaupt L, Spiecker M, Gusenkova D, Maleeva N, Skacel S T, Takmakov I, Valenti F, Winkel P, Rotzinger H, Wernsdorfer W *et al.* 2019 *Nat. Mater.* **18** 816–819
- [50] Winkel P, Borisov K, Grünhaupt L, Rieger D, Spiecker M, Valenti F, Ustinov A V, Wernsdorfer W and Pop I M 2020 *Phys. Rev. X* **10** 031032
- [51] Mukhanova E, Zeng W, Heredia E A, Wu C W, Lilja I, Lin J J, Yeh S S and Hakonen P 2024 *APL Materials* **12**